AFRL-RX-WP-TP-2011-4302

PERIPHERAL MILLING OF THIN TITANIUM PLATES: MODELING, ANALYSIS, AND PROCESS PLANNING (PREPRINT)

Robert Landers, Grzegorz Galecki, Keith Young, and Ryan Hanks

**Missouri University of Science and Technology
(formerly Missouri University – Rolla)**

JULY 2011

STINFO COPY

**AIR FORCE RESEARCH LABORATORY
MATERIALS AND MANUFACTURING DIRECTORATE
WRIGHT-PATTERSON AIR FORCE BASE, OH 45433-7750
AIR FORCE MATERIEL COMMAND
UNITED STATES AIR FORCE**

REPORT DOCUMENTATION PAGE		*Form Approved* *OMB No. 0704-0188*

The public reporting burden for this collection of information is estimated to average 1 hour per response, including the time for reviewing instructions, searching existing data sources, gathering and maintaining the data needed, and completing and reviewing the collection of information. Send comments regarding this burden estimate or any other aspect of this collection of information, including suggestions for reducing this burden, to Department of Defense, Washington Headquarters Services, Directorate for Information Operations and Reports (0704-0188), 1215 Jefferson Davis Highway, Suite 1204, Arlington, VA 22202-4302. Respondents should be aware that notwithstanding any other provision of law, no person shall be subject to any penalty for failing to comply with a collection of information if it does not display a currently valid OMB control number. **PLEASE DO NOT RETURN YOUR FORM TO THE ABOVE ADDRESS**.

1. REPORT DATE *(DD-MM-YY)*	2. REPORT TYPE	3. DATES COVERED *(From - To)*
July 2011	Journal Article Preprint	01 July 2011 – 01 July 2011

4. TITLE AND SUBTITLE	5a. CONTRACT NUMBER
PERIPHERAL MILLING OF THIN TITANIUM PLATES: MODELING, ANALYSIS, AND PROCESS PLANNING (PREPRINT)	FA8650-04-C-5704
	5b. GRANT NUMBER
	5c. PROGRAM ELEMENT NUMBER 62102F

6. AUTHOR(S)	5d. PROJECT NUMBER
Robert Landers, Grzegorz Galecki, Keith Young, and Ryan Hanks	4347
	5e. TASK NUMBER 00
	5f. WORK UNIT NUMBER 25100000

7. PERFORMING ORGANIZATION NAME(S) AND ADDRESS(ES)	8. PERFORMING ORGANIZATION REPORT NUMBER
Missouri University of Science and Technology (formerly Missouri University – Rolla) 1870 Miner Circle Rolla, MO 65409	

9. SPONSORING/MONITORING AGENCY NAME(S) AND ADDRESS(ES)	10. SPONSORING/MONITORING AGENCY ACRONYM(S) AFRL/RXLM
Air Force Research Laboratory Materials and Manufacturing Directorate Wright-Patterson Air Force Base, OH 45433-7750 Air Force Materiel Command United States Air Force	
	11. SPONSORING/MONITORING AGENCY REPORT NUMBER(S) AFRL-RX-WP-TP-2011-4302

12. DISTRIBUTION/AVAILABILITY STATEMENT
Approved for public release; distribution unlimited.

13. SUPPLEMENTARY NOTES
PAO Case Number: 88ABW 2010-5921; Clearance Date: 08 Nov 2010. Document contains color.

Journal article submitted to *Journal of Engineering Manufacture*.

14. ABSTRACT
This paper presents research conducted to model and analyze the peripheral milling of thin titanium plates. Impact tests are performed and the vibration characteristics of a thin titanium plate are modeled empirically. The force process is described by a mechanistic model and experimental data are used to determine the model parameters. The Particle Swarm Optimization technique is used to determine the parameters of the plate vibration and force process models, which are combined to create a complete model of the thin titanium plate peripheral milling operation. The models are validated experimentally and the results showed excellent agreement between the simulation and experimental results. A process planning scheme for peripheral milling of thin titanium plates is developed and applied. In this scheme, integer numbers of widths-of-cut and depths-of-cut are used and the optimal helix angle and feed are computed for each combination of width-of-cut and depth-of-cut. The process planning test case revealed the optimal material removal rate decreases as the width-of-cut decreases.

15. SUBJECT TERMS
peripheral milling, thin titanium plates

16. SECURITY CLASSIFICATION OF:			17. LIMITATION OF ABSTRACT:	18. NUMBER OF PAGES	19a. NAME OF RESPONSIBLE PERSON (Monitor)
a. REPORT Unclassified	b. ABSTRACT Unclassified	c. THIS PAGE Unclassified	SAR	44	Donna L. Ballard 19b. TELEPHONE NUMBER (Include Area Code) N/A

Standard Form 298 (Rev. 8-98)
Prescribed by ANSI Std. Z39-18

Peripheral Milling of Thin Titanium Plates:

Modeling, Analysis, and Process Planning

Abstract

This paper presents research conducted to model and analyze the peripheral milling of thin titanium plates. Impact tests are performed and the vibration characteristics of a thin titanium plate are modeled empirically. The force process is described by a mechanistic model and experimental data are used to determine the model parameters. The Particle Swarm Optimization technique is used to determine the parameters of the plate vibration and force process models, which are combined to create a complete model of the thin titanium plate peripheral milling operation. The models are validated experimentally and the results showed excellent agreement between the simulation and experimental results. A process planning scheme for peripheral milling of thin titanium plates is developed and applied. In this scheme integer numbers of widths–of–cut and depths–of–cut are used and the optimal helix angle and feed are computed for each combination of width–of–cut and depth–of–cut. The process planning test case revealed the optimal material removal rate decreases as the width–of–cut decreases, the optimal helix angle is independent of the width–of–cut, and the optimal feed increases as the width–of–cut decreases. The test case also revealed the optimal material removal rate is independent of depth–of–cut, the optimal helix angle increases as the depth–of–cut decreases, and the optimal feed increases as the depth–of–cut decreases.

1. Introduction

Due to its light weight and high strength, titanium is a critical material for a wide variety of aerospace components. Many of these components do not bear structural loads and are being designed to increasingly thinner specifications to further reduce weight and improve aircraft performance. A better understanding of the machining process is required. Therefore, this research seeks to 1) model the plate vibrations and machining forces for peripheral milling of thin titanium components, 2) validate the models experimentally, and 3) develop a process planning scheme for peripheral milling of thin titanium components.

Literature Review

There have been many studies, most of which are experimental in nature, that have investigated the machining of titanium alloys. Malone [1997] discussed machining tough materials including titanium and suggested using inserts with high positive rake angles and sharp cutting edges or light, precise hones. Many studies, such as that by Baeker *et al.* [2000], investigated chip formation. Barry *et al.* [2001] used acoustic emission (AE) to investigate the turning of Ti6Al4V and found that for high speeds the chip welded to the tool and fracture was the dominant source of the AE signal. Chen *et al.* [2002] investigated chip formation in high speed milling of titanium alloys and found a lack of chip deformation at high cutting speeds. There have been several studies of tool wear in titanium machining operations. Brinksmeier *et al.* [1999] investigated the use of mist lubrication when end milling Ti6Al4V and found it to be better than dry machining and as effective as flood coolant when using high speed steel tools. de Lacalle *et al.* [2000] investigated tool wear as a function of cutting speed, feed, and tool coatings when machining titanium. They concluded that TiCN coatings are preferable. Zoya and Krishnamurthy [2000]

conducted end milling experiments of a titanium alloy using PCBN tools and observed that 700°C is a critical temperature that can be a criterion for tool life, and cutting speed in the range of 185 to 220 m/min is recommended. Tool life can be improved by using liquid nitrogen for cryogenic machining of titanium [Hong *et al*., 2001a,b]. Tool life was also shown to improve when milling titanium compressor blades using a cooling refrigerant and a PCD tool [Kuljanic *et al*., 1998]. Corduan *et al*. [2003] investigated the wear mechanisms for machining titanium alloys when using polycrystalline diamond (PCD) tools, cubic crystalline boron nitride (CBN) tools, and TiB2 coated carbide tools. It was found that the different wear patterns are not only strongly linked to the chemical reactions, but also to the different phase changes, which occur when using PCD and CBN tools. Xu *et al*. [2004] used radial force frequency analysis to explore a monitoring method for flank wear and found that the amplitude of the fifth harmonic was very sensitive to flank wear. Wang *et al*. [2005] investigated the use of binderless CBN tool when high speed machining Ti6Al4V and found that workpiece adhesion and attrition are the main wear mechanisms. Another study by Shivpuri *et al*. [2002] investigated the microstructure, particularly cracking, of titanium parts after end milling with a variety of cutting conditions. Li *et al*. [2004] used embedded thermocouples to investigate cutting temperature when end milling titanium. They found the cutting temperature increased as the cutting speed increased. Li *et al*. [2007] investigated drilling operations for Ti6Al4V and found that high throughput drilling of Ti6Al4V is possible when using coolant, spiral point drill geometry, fine–grained WC–Co tool material, and the proper balance of feed and speed.

Several studies have modeled milling operations of thin–walled structures. Elbestawi and Sagherian [1991] conducted simulations to determine surface errors in the milling of thin–walled sections. The end mill was modeled as a cantilevered beam and the plate was simulated using the

Approved for public release; distribution unlimited.

Finite Element (FE) method. The study considered tool disengagement. Tsai and Liao [1999] investigated static surface errors of thin–walled parts in peripheral milling operations using the FE method to model both the end mill and the part. Static deformation of cantilevered plates was investigated by Aijun and Zhanqiang [2008] by considering the average cutting force acting on the plate. An analytical static deflection model was used to simulate the plate. Meshreki *et al.* [2008] created a simplified model, based on Rayleigh's energy method, to simulate milling operations of thin–walled structures. The FE method, coupled with impact tests, was used by Seguy *et al.* [2008] to create a model of milling operations for thin components. The model was used to investigate chatter and surface roughness. Process planning to regulate surface errors when machining thin–walled parts has also been considered. Budak and Altintas [1995] changed the tool immersion in the axial direction to regulate static form errors of plates in peripheral milling operations. The end mill was modeled as a cantilevered beam and the plate was simulated using the FE method. The effect of the work piece tilt angle on the surface error of thin cantilevered plates was investigated for traditional milling operations in Lee *et al.* [2003] and ball end milling operations in Lee *et al.* [2004]. Zhao *et al.* [2004] investigated controlling surface errors by tool path optimization including tilting the tool and using a combination of large and small axial and radial depths–of–cut. Ratchev *et al.* [2005] investigated the use of a tool profiled motion along the depth direction to achieve a constant width of removed material.

Experimental System

The machine tool used for the machining experiments conducted in this paper is a Cincinnati V–CNC 750 vertical machining center. The maximum spindle power is 17 hp and the maximum spindle speed is 8000 rpm. The travel in the *x*, *y*, and *z* directions are 762, 508, and 508 mm,

respectively, and the maximum cutting feedrate is 250 mm/s. A solid–carbide, eight–flute end mill was utilized in all of the machining experiments. The tool has a helix angle of 40°, a radius of 9.525 mm, and a corner radius of 3.048 mm.

To measure machining forces during the operations, a 3–axis dynamometer (Kistler 9257BA) was utilized. The ranges are ±5 kN in the x direction (parallel to the plate in the horizontal direction), ±5 kN in the y direction (perpendicular to the plate), and ±10 kN in the z direction (parallel to the plate in the vertical direction). The natural frequencies for the x and y directions are 2.0 kHz and the natural frequency for the z direction is 3.5 kHz. The amplifier was equipped with 2.0 kHz low pass filters for all three directions. To measure plate vibrations during machining operations, eddy current displacement sensors (Lion Precision ECL 100–U5B) were utilized. The sensors are specifically calibrated for titanium, have an offset of 0.25 mm, a range of 1.25 mm, a bandwidth of 80 kHz, and a resolution of 0.75 µm. To determine cutting tool and plate structural dynamics, an impact hammer (PCB Piezotronics 086C03) was utilized. The sensitivity is 2.25 mV/N, the range is ±2.2 kN, and the –10 dB frequency range is 8 kHz.

A National Instruments (NI) PCI–6040E multifunction card was utilized to measure data during the machining experiments and for the structural modeling experiments. The multifunction card has sixteen single–ended (eight double–ended) analog inputs. The maximum input rate is 500 kS/s with an operation range from ±0.05 to ±10 V.

A special fixture to machine thin plates of various thicknesses was constructed (see Figure 1). The fixture is attached to a dynamometer for machining force measurements. Eddy current sensors are placed on the side of the fixture, opposite to the machined surface, for plate vibration monitoring during machining (see Figure 1).
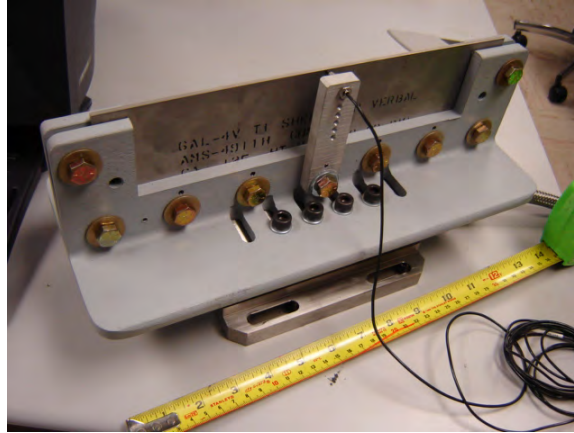
Figure 1: Fixture Mounted to Kistler Dynamometer. Eddy Current Sensors can be Placed at Different Vertical Positions with Increments of 6.35 mm and Five Different Horizontal Locations. Machining Occurs on the Opposite Side of the Plate.

Particle Swarm Optimization

Particle Swarm Optimization (PSO), a method based on the concept of social interactions such as bird flocking and fish schooling [Kennedy and Eberhart, 1995], is used in this work to develop models of the thin titanium peripheral milling operation. Given measurement data, model parameters are optimized such that the difference between the model outputs and corresponding measurement data is minimized.

The algorithm utilizes the following steps. First, the model structure is determined. The model contains n_p unknown model parameters. Then, the parameters of n_s model parameter sets are randomly populated. Each model parameter is bounded by minimum and maximum values. Each model set is referred to as a particle. Next, changes in the model parameters for each parameter are randomly selected. These changes are also bounded by minimum and maximum values. The cost function of each of the n_s model parameter sets is evaluated in the next step. The cost function is a user defined function that describes how well the model set fits the given

experimental data. Then, the cost functions for the n_s model parameter sets are compared and the model parameter set with the minimum cost function is determined. This model parameter set is the global best model parameter set. Also, the model parameters of the global best model parameter set are the global best model parameters.

The PSO algorithm is implemented for a fixed number of iterations. The value of the jth model parameter in the ith model parameter set (x_{ij}) at the kth iteration is

$$x_{ij}(k) = x_{ij}(k-1) + v_{ij}(k) \qquad i = 1, \ldots, n_s \quad j = 1, \ldots, n_p \tag{1}$$

where v_{ij} is the change in the jth model parameter in the ith model parameter set at the kth iteration and is

$$v_{ij}(k) = w(k)v_{ij}(k-1) + c_1 r_1(k)\left[p_{ij}(k-1) - x_{ij}(k-1)\right] \\ + c_2 r_2(k)\left[p_{gj}(k-1) - x_{ij}(k-1)\right] \qquad i = 1, \ldots, n_s \quad j = 1, \ldots, n_p \tag{2}$$

The subscripts i and j refer to the ith model parameter set and the jth model parameter, respectively. The parameter $w(k)$ is known as the inertial weight, the parameters c_1 and c_2 are user selected constants ($c_1 = c_2 = 2$ in this study), and the parameters $r_1(k)$ and $r_2(k)$ are random numbers, evenly distributed between 0 and 1, determined at each iteration. The parameter p_{ij} is the best j^{th} model parameter in the ith model parameter set and p_{gj} is the jth model parameter in the global best model parameter set. Therefore, the PSO algorithm changes each model parameter according to the previous change in the model parameter, the difference between the model parameter and the best parameter in its model parameter set, and the difference between the model parameter and the global best model parameter of all of the model parameter sets. If the model parameters and changes in model parameters exceed their minimum or maximum values, they are set equal to their minimum or maximum values, respectively

$$\text{if} \quad x_{ij}(k) < x_j^{\min} \quad \text{then} \quad x_{ij}(k) = x_j^{\min} \qquad i = 1, \ldots, n_s \quad j = 1, \ldots, n_p \tag{3}$$

$$\text{if} \quad x_{ij}(k) > x_j^{\max} \quad \text{then} \quad x_{ij}(k) = x_j^{\max} \qquad i = 1,\ldots,n_s \quad j = 1,\ldots,n_p \tag{4}$$

$$\text{if} \quad v_{ij}(k) < v_j^{\min} \quad \text{then} \quad v_{ij}(k) = v_j^{\min} \qquad i = 1,\ldots,n_s \quad j = 1,\ldots,n_p \tag{5}$$

$$\text{if} \quad v_{ij}(k) > v_j^{\max} \quad \text{then} \quad v_{ij}(k) = v_j^{\max} \qquad i = 1,\ldots,n_s \quad j = 1,\ldots,n_p \tag{6}$$

The inertial weight linearly decreases from its maximum ($w_{\max}$) to its minimum ($w_{\min}$) value and is

$$w(k) = w_{\max} - k \frac{w_{\max} - w_{\min}}{k_{\max}} \tag{7}$$

where the parameter $k_{\max}$ is the maximum number of iterations. Equations (1)–(7) are implemented until $k = k_{\max}$. Since the PSO method is not gradient based, it is capable of escaping local minima and finding the global minimum.

2. Plate Dynamic Modeling

The structural response of a thin titanium plate (254 mm in length, 50.8 mm in height, and 3.378 mm thick) was modeled experimentally. The plate was mounted in the special fixture (see Figure 1). The plate was clamped on the bottom and both sides, and was free on the top. Ten impact tests were conducted at fifteen locations (see Figure 2). For each test, the eddy current sensor was mounted on one side of the plate, and the plate was struck on the other side with the impact hammer directly opposite to the sensor. The impact hammer force and eddy current displacement signals were sampled simultaneously at a frequency of 10 kHz. Each data set was windowed such that 500 total points (10 before the impact and 490 subsequent to the impact) were selected for analysis. For each data set, the displacement and force signals were transformed into the frequency domain using the Matlab **fft** command.
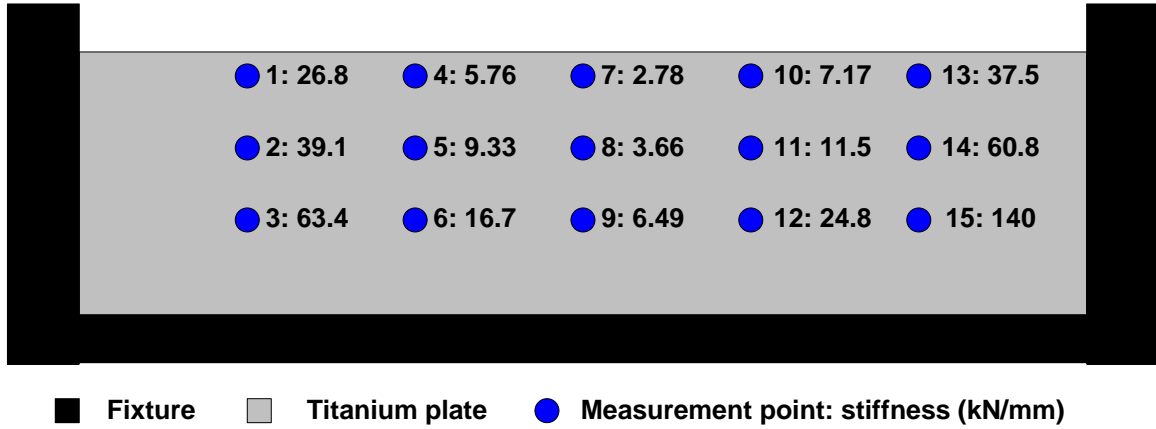
Figure 2: Titanium Plate (3.378 mm thickness) Static Stiffnesses.

The magnitude frequency responses at the frequencies of 20, 40, 60, 80, 100, 120, 140, 160, 180, and 200 Hz were averaged at each location. These fifteen values were inverted to determine the static stiffnesses, in units of kN/mm, at each location and the results are shown in Figure 2. The magnitude frequency response at 0 Hz was not considered since the values at this frequency tend to be distorted due to small biases in the eddy current sensor signal. As expected, the static stiffness is minimal at the top, middle location and increases for locations closer to the fixture. The static stiffnesses are not symmetric about the plate's vertical centerline since the measurement locations are slightly shifted to the right side.

A model tailored to location 7 is used for subsequent simulations. This location is the critical point since the plate static stiffness is minimal at this location. The proposed model is

$$\frac{D_7(s)}{F(s)} = \frac{k_7^{-1}\left(\dfrac{s^2}{\omega_{z1}^2} + \dfrac{2\zeta_{z1}s}{\omega_{z1}} + 1\right)\cdots\left(\dfrac{s^2}{\omega_{z3}^2} + \dfrac{2\zeta_{z3}s}{\omega_{z3}} + 1\right)}{\left(\dfrac{s^2}{(2\pi960)^2} + \dfrac{2\zeta_{p1}s}{2\pi960} + 1\right)\cdots\left(\dfrac{s^2}{(2\pi3160)^2} + \dfrac{2\zeta_{p4}s}{2\pi3160} + 1\right)} \tag{8}$$

where D_7 is the plate deflection at location 7, $k_7 = 2.78$ kN/mm, the four identified natural frequencies for the poles are 960, 1280, 1740, and 3160 Hz, and the parameters ζ_{z1}, ζ_{z2}, ζ_{z3}, ω_{z1}, ω_{z2}, ω_{z3}, ζ_{p1}, ζ_{p2}, ζ_{p3}, and ζ_{p4}, are determined by applying PSO. The cost function is the sum of the square of the differences between the experimental and model magnitudes for frequencies from 0 to 3580 Hz. The data for frequencies above 3580 Hz are not considered since there is uncertainty in the frequency response near the sampling bandwidth. The damping ratios are bounded between 10^{-10} and 0.2, and the natural frequencies for the zeros are bounded as follows: $960 \leq \omega_{z1} \leq 1280$ rad/s, $1280 \leq \omega_{z2} \leq 1740$ rad/s, and $1740 \leq \omega_{z3} \leq 3160$ rad/s. The maximum changes in the damping ratios are bounded by ± 0.01 and the maximum changes in the natural frequencies are bounded by ± 10 rad/s. The algorithm utilizes 500 model parameter sets and executes 1000 iterations. The damping ratios of the best model parameter set at each iteration are shown in Figure 3. These parameters remain constant after 600 iterations and are $\zeta_{z1} = 1.63 \cdot 10^{-2}$, $\zeta_{z2} = 4.43 \cdot 10^{-2}$, $\zeta_{z3} = 1.10 \cdot 10^{-3}$, $\zeta_{p1} = 8.64 \cdot 10^{-3}$, $\zeta_{p2} = 1.68 \cdot 10^{-2}$, $\zeta_{p3} = 6.42 \cdot 10^{-3}$, and $\zeta_{p4} = 4.21 \cdot 10^{-3}$. The natural frequencies of the best model parameter set at each iteration are shown in Figure 4. These parameters remain constant after 200 iterations and are $\omega_{z1} = 1190$ rad/s, $\omega_{z2} = 1540$ rad/s, and $\omega_{z3} = 2760$ rad/s. The natural frequencies tend to converge more quickly than the damping ratios since the range of the natural frequencies are bounded more tightly. The cost function at each iteration is also shown in Figure 4. Since the model parameters are well–bounded, the initial cost function was close to the final cost function. The cost function decreases quickly as the natural frequencies converge and then decrease slowly until the damping ratios converge.
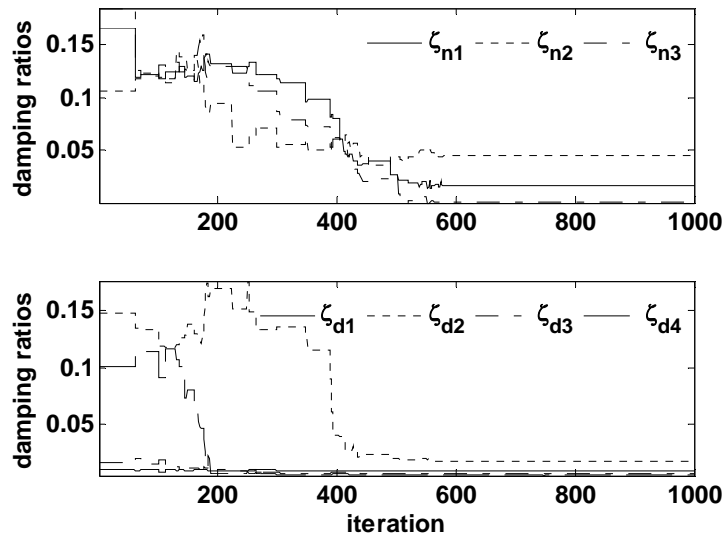
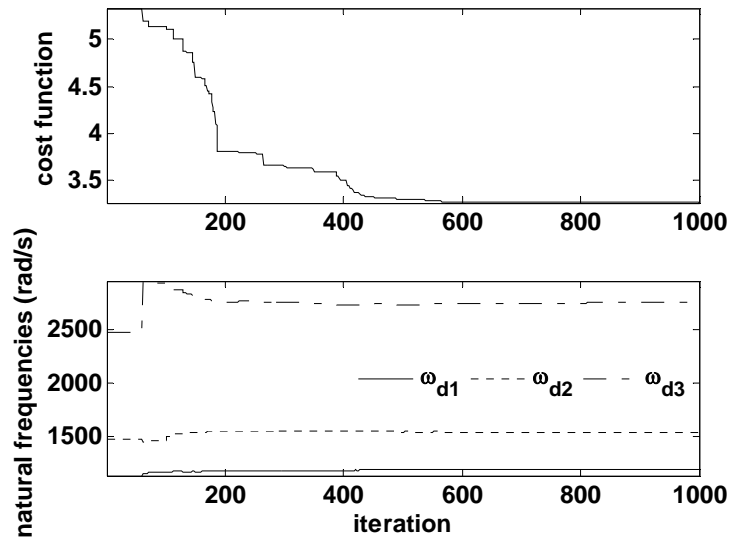**Figure 3: Evolution of Best Structural Model Damping Ratios.**

Figure 4: Evolution of Structural Model Best Cost Function (top) and Best Structural

Model Natural Frequencies (bottom).

The experimental and model magnitude frequency responses at location 7 are shown in Figure 5. The model magnitude frequency response matches the experimental magnitude

frequency response very well over all frequencies, except those near 5000 Hz, which is due to uncertainty in the frequency response near the sampling bandwidth. Figure 6 shows simulation and experimental results for an impact test. The results show the model captures the force frequency and magnitude very well. It should be noted that the fixturing (i.e., specific clamping force distribution) will affect the plate dynamic model; therefore, each plate will have slightly different dynamic model.
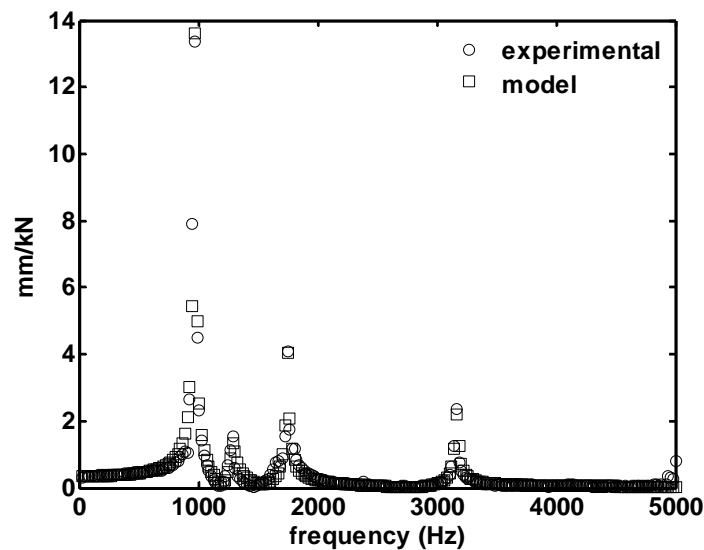
Figure 5: Model versus Experimental Magnitude Frequency Response at Location 7.
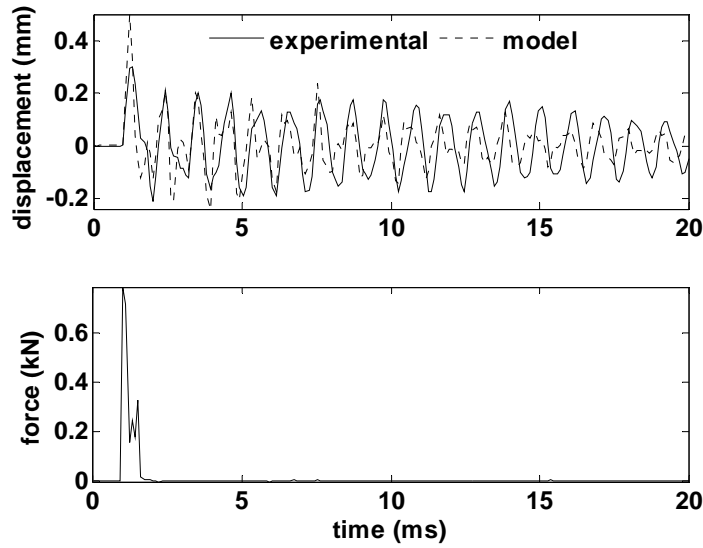
Figure 6: Experimental and Modeled Displacements at Location 7 for Impact Test.

3. Force Process Modeling

Machining experiments were conducted on a titanium block to determine cutting force model parameters. Nine experiments, listed in Table 1, were selected for machining force process modeling. For all nine experiments the spindle speed and depth–of–cut were N_s = 1350 rpm and d = 12.7 mm, respectively, the feed/flute varied such that $0.051 \leq f_f \leq 0.102$ mm, and the width– of–cut varied such that $1.27 \leq w \leq 2.54$ mm. This range is typical of traditional milling, as opposed to high speed milling, of titanium. The experimental results for Case 1 (N_s = 1350 rpm, d = 12.7 mm, f_f = 0.051 mm, and w = 1.27 mm) in Table 1 are shown in Figure 7. The figure shows the forces acting on the part in the x (parallel to the plate in the horizontal direction), y (perpendicular to the plate), and z (parallel to the plate in the vertical direction) directions. The forces are shown for five spindle revolutions in the x direction and twenty–three revolutions in the y and z directions. Figure 7 also shows the PSD for these force signals. The time plots do not

start at time zero since cutting data was presented only from the middle of the cut to show steady cutting conditions. In Figure 7, there is significant energy at 22.5 Hz and 180 Hz, which are the tool rotation and flute passing frequencies, respectively, for this experiment. The y and z force signals illustrate the repeatability of the force process during each tool rotation. The x force signal illustrates the force variation during each flute rotation. The variation in the x force signal from flute to flute indicates a slight tool eccentricity was present.

Table 1: Process Parameters and Mean Machining Forces for Machining Experiments Used to Develop Machining Force Model ($N_s = 1350$ rpm and $d = 12.7$ mm).

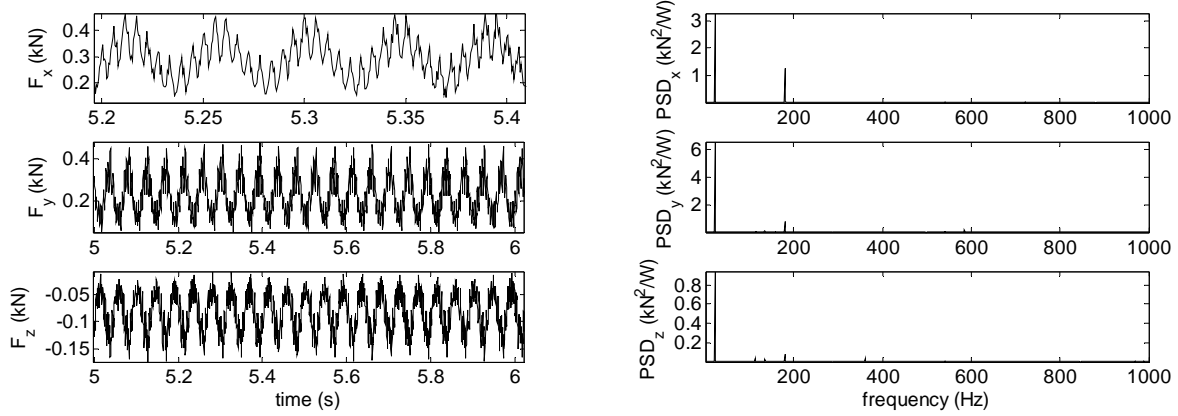| Case	f_f (mm)	w (mm)	$\bar{F}_x$ (N)	$\bar{F}_y$ (N)	$\bar{F}_z$ (N)
1	0.051	1.27	232	−291	−83.0
2	0.051	1.905	304	−409	−118
3	0.051	2.54	366	−538	−156
4	0.076	1.27	337	−376	−127
5	0.076	1.905	442	−524	−181
6	0.076	2.54	534	−688	−246
7	0.102	1.27	436	−457	−173
8	0.102	1.905	572	−634	−250
9	0.102	2.54	697	−851	−344

Figure 7: Machining Forces acting on Tool and Power Spectral Densities of these Signals (Case 1 in Table 1: N_s = 1350 rpm, f_f = 0.051 mm/flute, w = 1.27 mm, d = 12.7 mm). The signal F_x is Shown for Five Tool Revolutions. The signals F_y and F_z are Shown for Twenty–Three Tool Revolutions.

To model the end milling process the end mill is sliced into disks with height Δz (see Figures 8 and 9). In these studies up milling, as opposed to the more conventional down milling, is used. In up milling, the chip load on the flute gradually increases from zero to the full chip load during the flute's revolution. The helix angle is assumed to be zero for each slice. Each disk is analyzed like a face mill. The disk at the bottom of the end mill will be analyzed first. The instantaneous feed of the bottom disk of the ith flute is

$$f_i = f_f \cos(\theta_i) \tag{9}$$

where f_f is the feed/flute and θ_i is the angle of the ith flute measured in the x–y plane from the positive x direction to the flute, with clockwise as the positive direction. The corresponding chip area of the bottom disk of the ith flute is

$$a_i = f_i \Delta z \cos(\theta_i) \tag{10}$$

The cutting, thrust, and lateral forces, respectively, acting on the bottom disk of the ith flute are

$$F_{C_i} = P_C a_i \tag{11}$$

$$F_{T_i} = P_T a_i \tag{12}$$

$$F_{L_i} = P_L a_i \tag{13}$$

The forces acting on the bottom disk of the ith flute in the Cartesian coordinate system are

$$F_{x_i} = -F_{T_i} \cos(\theta_i) - F_{C_i} \sin(\theta_i) \tag{14}$$

$$F_{y_i} = -F_{T_i} \sin(\theta_i) + F_{C_i} \cos(\theta_i) \tag{15}$$

$$F_{z_i} = -F_{L_i} \tag{16}$$

The total forces acting on the bottom disk are

$$F_x = \sum_{i=1}^{N_f} \left[-F_{T_i} \cos(\theta_i) + F_{C_i} \sin(\theta_i) \right] \sigma(\theta_i) \tag{17}$$

$$F_y = \sum_{i=1}^{N_f} \left[-F_{T_i} \sin(\theta_i) - F_{C_i} \cos(\theta_i) \right] \sigma(\theta_i) \tag{18}$$

$$F_z = \sum_{i=1}^{N_f} \left[-F_{L_i} \right] \sigma(\theta_i) \tag{19}$$

where

$$\sigma(\theta_i) = \begin{cases} 0 & \text{if} & \theta_i < \theta_{ex} \\ 0 & \text{if} & \theta_{en} < \theta_i \\ 1 & \text{if} & \theta_{en} \geq \theta_i \geq \theta_{ex} \end{cases} \tag{20}$$

The function $\sigma(\theta_i)$ determines if the ith flute of bottom disk is in contact with the part. The entry and exit angles are determined by the end mill and part geometries. For the end milling tests conducted in this paper (see Figure 8), the entry and exit angles, respectively, are

$$\theta_{en} = \frac{\pi}{2} \tag{21}$$

$$\theta_{ex} = \frac{\pi}{2} - \cos^{-1}\left(\frac{R_t - w}{R_t}\right) \tag{22}$$

To determine the total forces acting on the end mill, the forces acting on each disk are summed

$$F_x = \sum_{j=1}^{N_d} \sum_{i=1}^{N_f} \left\{-F_T(i,j)\cos\left[\theta(i,j)\right] - F_C(i,j)\sin\left[\theta(i,j)\right]\right\}\sigma\left[\theta(i,j)\right] \tag{23}$$

$$F_y = \sum_{j=1}^{N_d} \sum_{i=1}^{N_f} \left\{-F_T(i,j)\sin\left[\theta(i,j)\right] + F_C(i,j)\cos\left[\theta(i,j)\right]\right\}\sigma\left[\theta(i,j)\right] \tag{24}$$

$$F_z = \sum_{j=1}^{N_d} \sum_{i=1}^{N_f} \left\{-F_L(i,j)\right\}\sigma\left[\theta(i,j)\right] \tag{25}$$

where N_d is the number of axial disks. The angle of the ith flute at the jth disk (see Figure 9) is

$$\theta(i,j) = \theta_i - (j-1)\frac{1}{R_t}\Delta z \tan\left(\gamma_p\right) \tag{26}$$

where θ_i is the angle of the ith flute on the bottom disk, R_t is the tool radius, and γ_p is the helix angle.
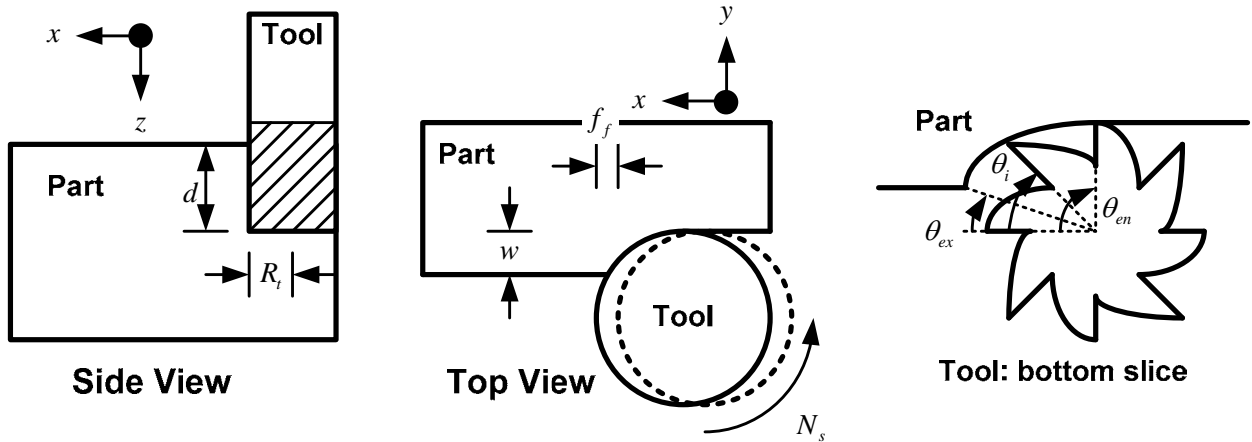
Figure 8: End Milling Schematics. Dotted Line is Tool's Path during Previous Rotation.
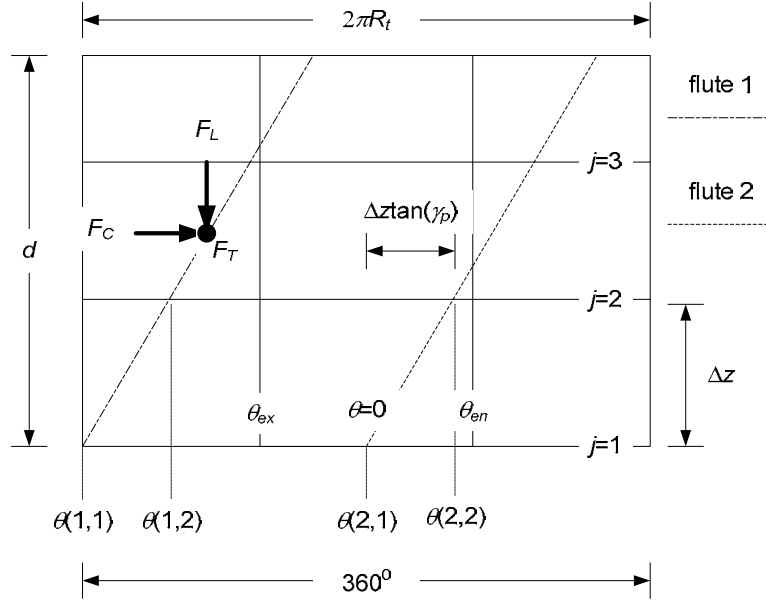
Figure 9: Two Dimensional View of End Mill.

The PSO method is utilized to determine the force process model coefficients (i.e., K_C, K_T, and K_L). The mean values for the x, y, and z forces were computed for the nine experiments in Table 1. For each iteration of the PSO algorithm, ten combinations of model parameters were simulated for all nine cutting conditions and their values were updated according to the PSO algorithm. The model parameters were bounded by ±10 kN/mm^2 and the changes in model parameters at each iteration were bounded by ±1 kN/mm^2. The performance index is the sum of the squares of the errors between the measured and modeled x, y, and z mean forces for all nine tests. Figure 10 shows the best performance index for all one hundred iterations. Note the performance index is plotted on a base 10 logarithmic scale. The index decreases in a step wise manner every time the PSO algorithm finds an improved solution. Figure 11 shows the best parameter values at each iteration. The parameter values change significantly at first and then converge close to their final values after approximately sixty iterations. The final values are $K_C =$ 1.14 kN/mm^2, $K_T = 2.49$ kN/mm^2, and $K_L = 0.759$ kN/mm^2. Typically, the cutting coefficient is

the largest of the three model coefficients; however, the data is somewhat weighted since the widths–of–cut are small. Figure 12 shows a plot of the measured versus modeled x, y, and z mean forces for the nine sets of data used to create the model. Note the solid line denotes perfect prediction. The average absolute values of the percent errors for these nine tests are 12.1%, 3.27%, and 3.06% for the x, y, and z forces, respectively. Thirteen tests (shown in Table 2), none of which were used to create the model, are used for validation. Figure 13 shows a plot of the measured versus modeled x, y, and z mean forces for the thirteen sets of data used to validate the model. Note the solid line denotes perfect prediction. The average absolute values of the percent errors for the thirteen tests are 13.6%, 3.00%, and 5.35% for the x, y, and z forces, respectively.
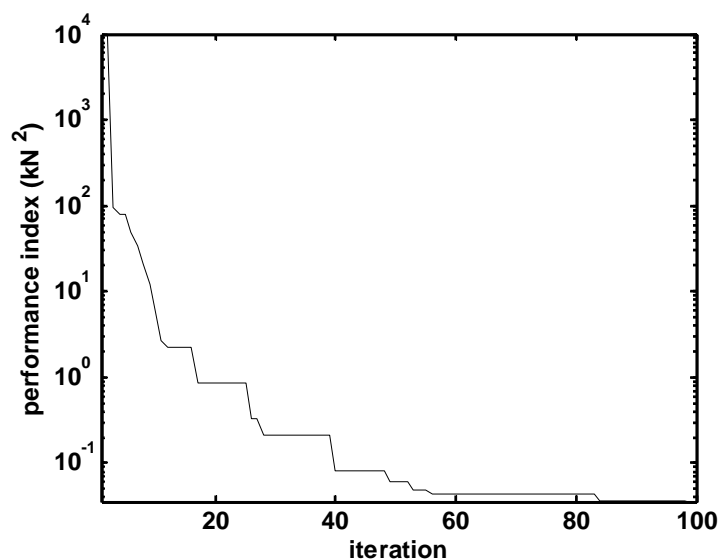
Figure 10: Evolution of Force Model Best Performance Index. Note Performance Index is Plotted on a Base 10 Logarithm Scale.
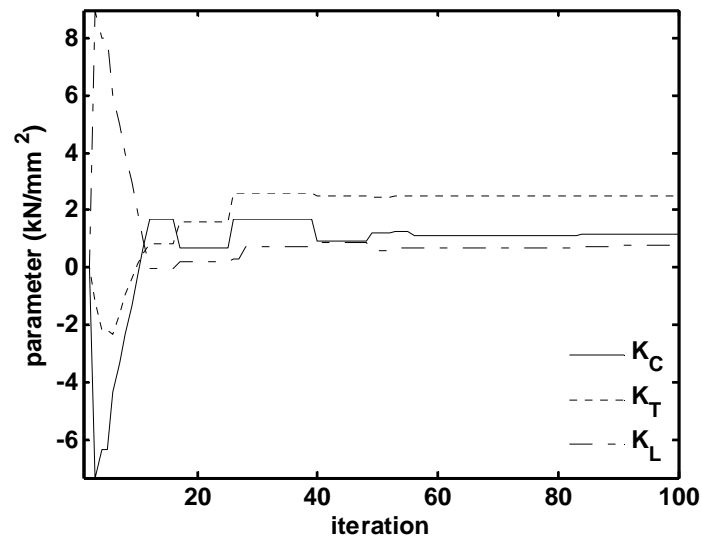
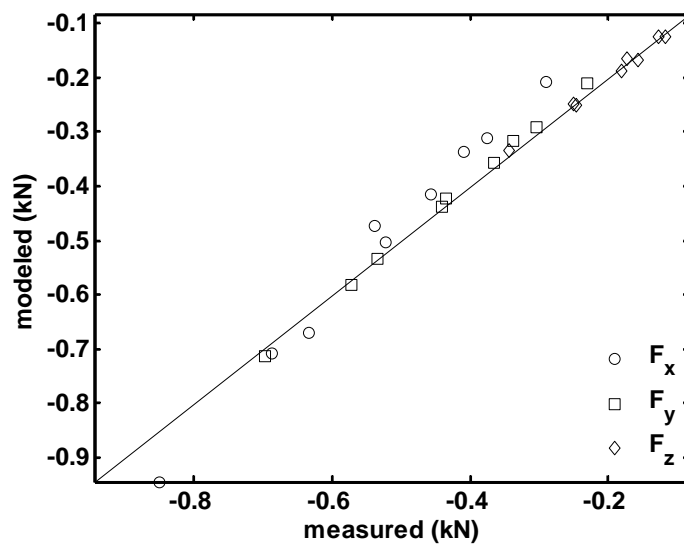**Figure 11: Evolution of Best Force Model Best Model Parameters.**

Figure 12: Measured versus Modeled Mean Force for Data in Table 1. Straight Line Denotes Perfect Prediction.
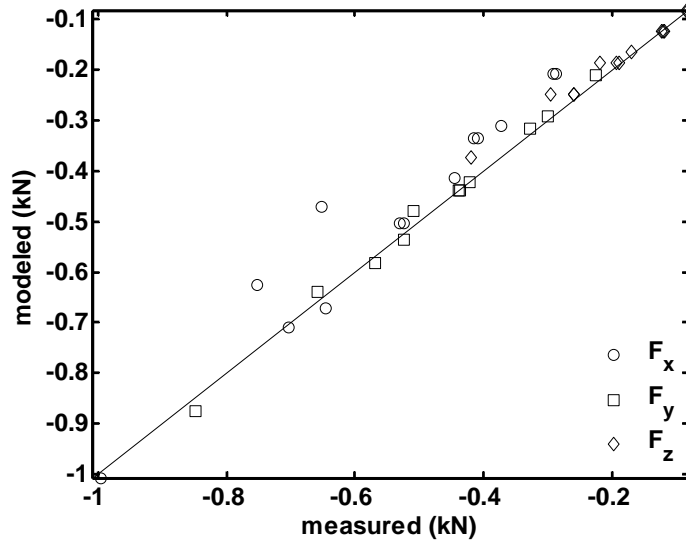
Figure 13: Measured versus Modeled Mean Force for Data in Table 2. Straight Line Denotes Perfect Prediction.

Table 2: Process Parameters and Mean Machining Forces for Machining Experiments Used to Validate Machining Force Model.

Case	N_s (rpm)	f_f (mm)	w (mm)	d (mm)	$\bar{F}_x$ (N)	$\bar{F}_y$ (N)	$\bar{F}_z$ (N)
1	1550	0.051	1.27	12.7	226	−288	−85.3
2	1750	0.051	1.27	12.7	225	−293	−81.8
3	1550	0.051	1.905	12.7	301	−409	−120
4	1750	0.051	1.905	12.7	300	−416	−120
5	1750	0.076	1.27	12.7	328	−372	−123
6	1550	0.076	1.905	12.7	438	−523	−193
7	1750	0.076	1.905	12.7	437	−531	−189
8	1750	0.076	2.54	12.7	525	−704	−260
9	1750	0.102	1.27	12.7	422	−446	−171
10	1750	0.102	1.905	12.7	569	−645	−261
11	1350	0.076	1.27	19.05	509	−652	−220
12	1350	0.102	1.27	19.05	659	−751	−295
13	1350	0.102	1.905	19.05	847	−996	−420

4. Model Validation

The machining force model developed in Section 3 is used to simulate the titanium end milling process for Cases 3, 5, and 13 in Table 2, and results are compared to the corresponding experimental data. The simulated and experimental machining forces for one tool rotation for Cases 3, 5, and 13 are shown in Figures 14, 15, and 16, respectively. The model predicts the shape of the force profiles and the force average values very well. However, the experimental data has some variation that is due to structural deflections, which are not included in the model. This is very apparent for Case 13. This case represented extreme cutting conditions in that the feed and depth–of–cut were at their respective maximum values and the width–of–cut was at its middle value.
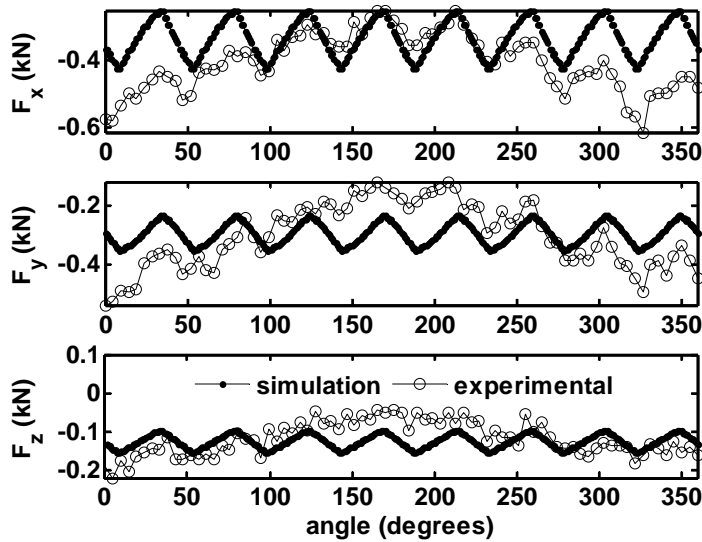
Figure 14: Simulated and Experimental Machining Forces for Case 3 in Table 2: $N_s = 1550$ **rpm,** $f = 0.051$ **mm/flute,** $w = 1.905$ **mm, and** $d = 12.7$ **mm.**
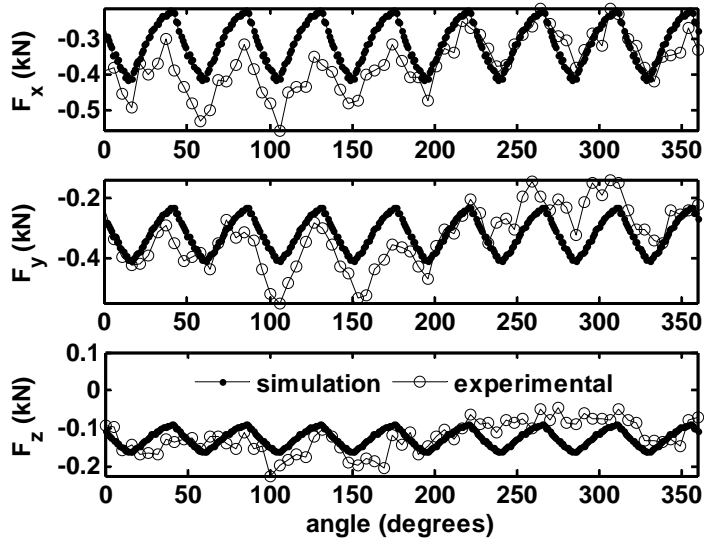
Figure 15: Simulated and Experimental Machining Forces for Case 5 in Table 2: N_s = 1750 rpm, f = 0.076 mm/flute, w = 1.27 mm, and d = 12.7 mm.
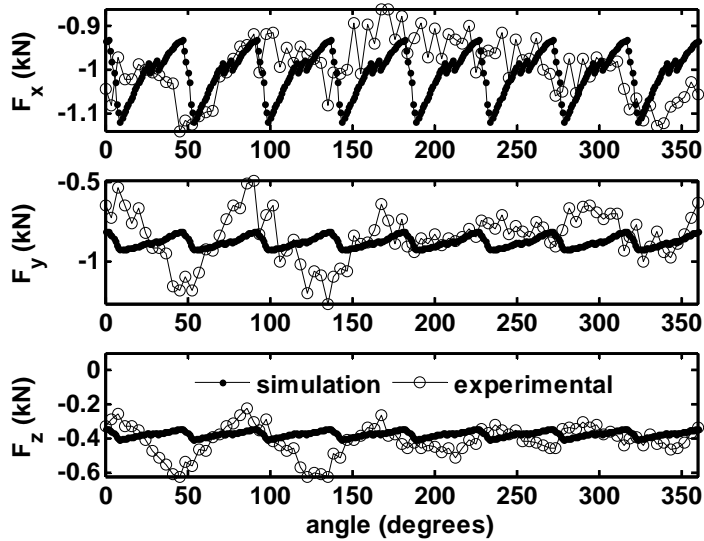

Figure 16: Simulated and Experimental Machining Forces for Case 13 in Table 2: N_s = 1350 rpm, f = 0.102 mm/flute, w = 1.905 mm, and d = 19.05 mm.

The plate dynamic structural model for the top middle location and the machining force process model are used to simulate the titanium end milling process, and the simulation and experimental results are compared. The simulations are known as Time Domain Simulations [Tsai *et al*., 1990; Smith and Tlusty, 1993; Weck *et al*., 1994]. Results are shown in Figures 17 and 18. These figures show, for one spindle rotation, the three machining forces and the plate structural displacement at the top, middle location as the tool was passing this location. In both figures it can be seen that the simulated forces and displacements predict the general shape of the experimental data very well. For the results shown in Figure 17, the simulated x forces slightly over predict the experimental data and, for the results shown in Figure 18, the simulated x forces slightly under predict the experimental data. The magnitude of the simulated y forces is very similar to the experimental data for both machining operations. The simulated z forces for both machining operations predict the average experimental data very well; however, the experimental data had substantially more variation than the simulated data. The simulated displacements predict the variation in the experimental displacements very well for the results shown in Figure 17 and slightly over predict the variations in the experimental displacements for the results shown in Figure 18. The simulated displacements are also slightly larger than the experimental data for both machining operations. This deviation is likely due to the fact that the plate stiffness characteristics slightly change every time a new plate is fixtured.
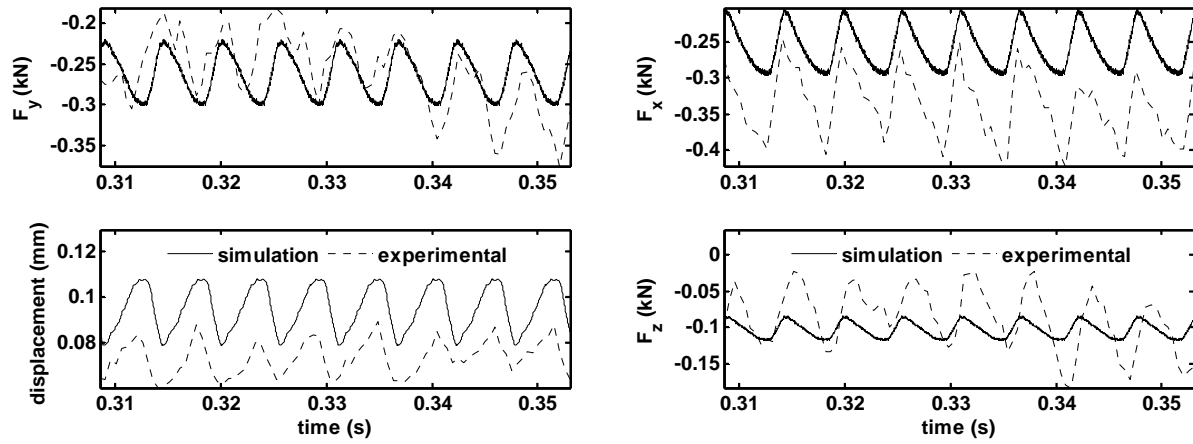
Figure 17: Time Domain Simulation versus Experimental Results for Machining Titanium 3.378 mm Thick Plate: N_s = 1350 rpm, f_f = 0.051 mm/flute, w = 1.27 mm, and d = 15.75 mm.
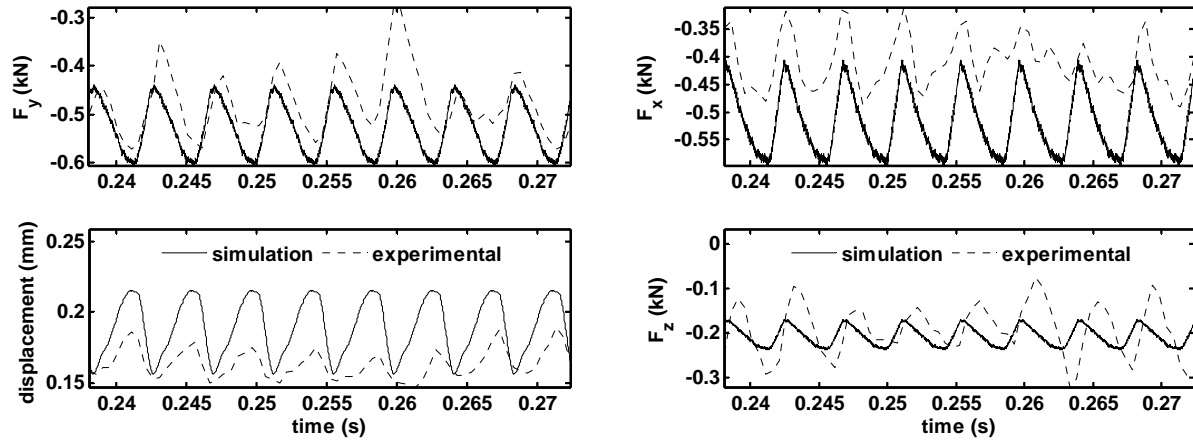

Figure 18: Time Domain Simulation versus Experimental Results for Machining Titanium 3.378 mm Thick Plate: N_s = 1750 rpm, f_f = 0.102 mm/flute, w = 1.27 mm, and d = 15.75 mm.

5. Peak–to–Peak y Force

The effect of width–of–cut, depth–of–cut, and helix angle on the peak–to–peak y force is investigated in this section. For helix angles of 5°, 20°, 35°, and 50° the machining process is simulated, without structural vibrations, and the maximum of the absolute value of the y force and the peak–to–peak y force are computed for a range of widths–of–cut from 0.254 to 3.048 mm and a range of depths–of–cut from 2.54 to 30.48 mm. The spindle speed is 1750 rpm, the tool radius is 9.525 mm, the number of flutes is 8, and the feed is 0.051 mm/flute. For each helix angle, three–dimensional plots showing the maximum of the absolute value of the y force and the peak–to–peak y force as functions of the width–of–cut and the depth–of–cut are constructed. The results are shown in Figures 19, 20, 21, and 22 for helix angles of 5°, 20°, 35°, and 50°, respectively. For all helix angles, the maximum of the absolute value of the y force monotonically increases with increasing width–of–cut and increasing depth–of–cut. For a helix angle of 5° the peak–to–peak y force increases as the depth–of–cut increases; however, the peak–to–peak y force first increases and then decreases as the width–of–cut increases. This trend with respect to the width–of–cut is the same for all four helix angles considered in this study. For a helix angle of 20° the peak–to–peak y force increases, decreases, and then increases again as the depth–of–cut increases. The valley seen in the peak–to–peak y force plot in Figure 20 indicates the depth–of–cut can be adjusted such that the peak–to–peak y force is very small. For helix angles of 35° and 50°, the peak–to–peak y force plots have two and four valleys, respectively, indicating the depth–of–cut can be adjusted to multiple values to achieve a very small peak–to–peak y force. If the peak–to–peak y force plots were extended in the width–of–cut direction, it would be seen that there are valleys in this direction, too.
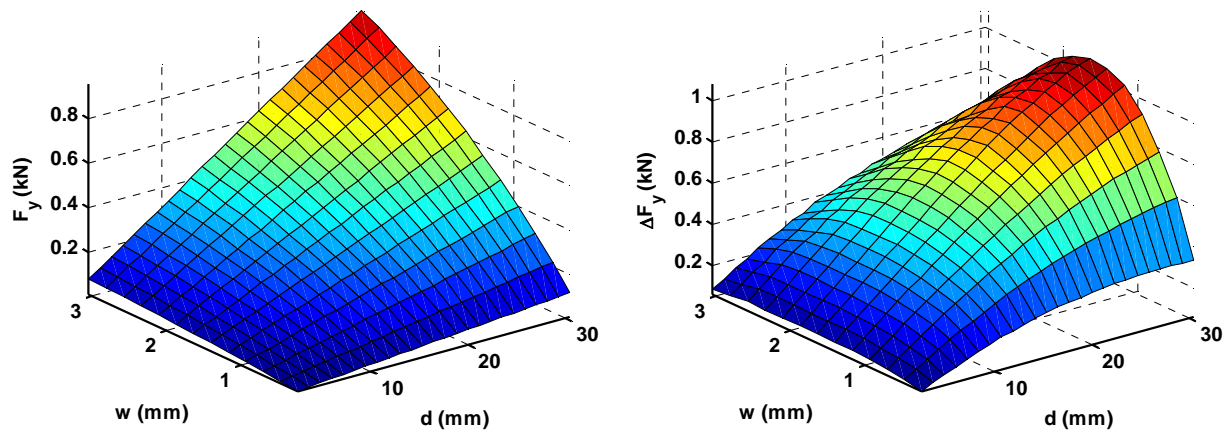
Figure 19: Maximum Absolute Value of *y* Force (left) and Peak–to–Peak *y* Force (right) as Functions of Width–of–Cut and Depth–of–Cut: N_s = 1750 rpm, N_f = 8, R_t = 9.525 mm, f_f = 0.051 mm/flute, and γ_r = 5°.
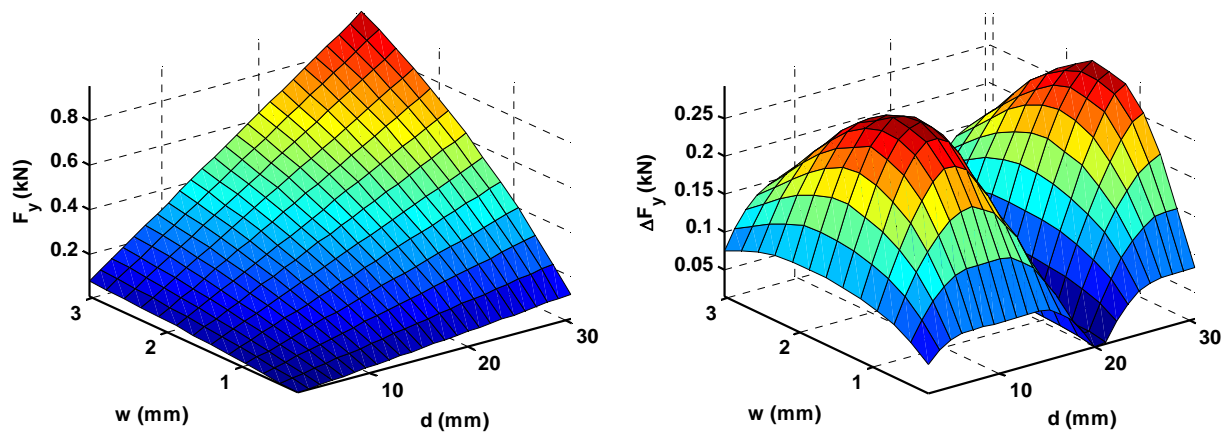

Figure 20: Maximum Absolute Value of *y* Force (left) and Peak–to–Peak *y* Force (right) as Functions of Width–of–Cut and Depth–of–Cut: N_s = 1750 rpm, N_f = 8, R_t = 9.525 mm, f_f = 0.051 mm/flute, and γ_r = 20°.
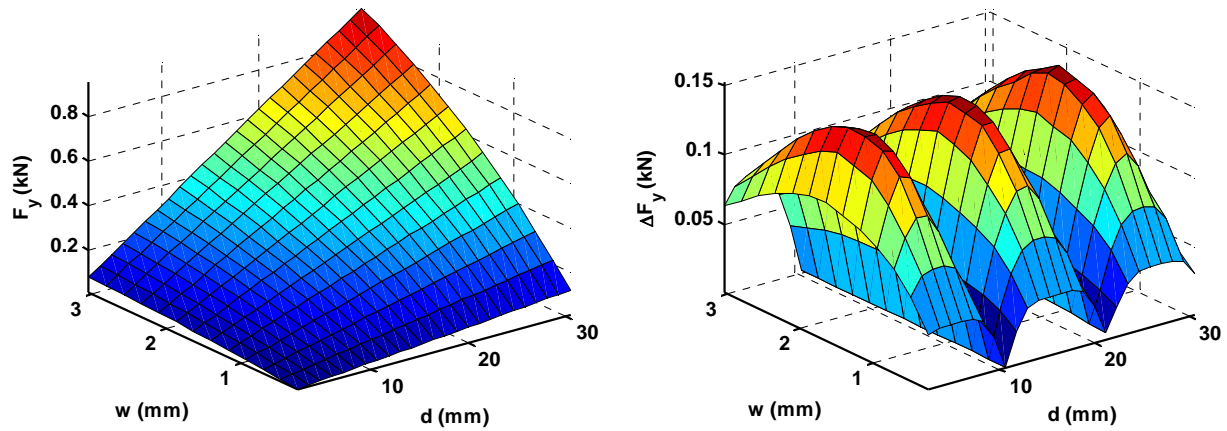
Figure 21: Maximum Absolute Value of *y* Force (left) and Peak–to–Peak *y* Force (right) as Functions of Width–of–Cut and Depth–of–Cut: N_s = 1750 rpm, N_f = 8, R_t = 9.525 mm, f_f = 0.051 mm/flute, and γ_r = 35°.
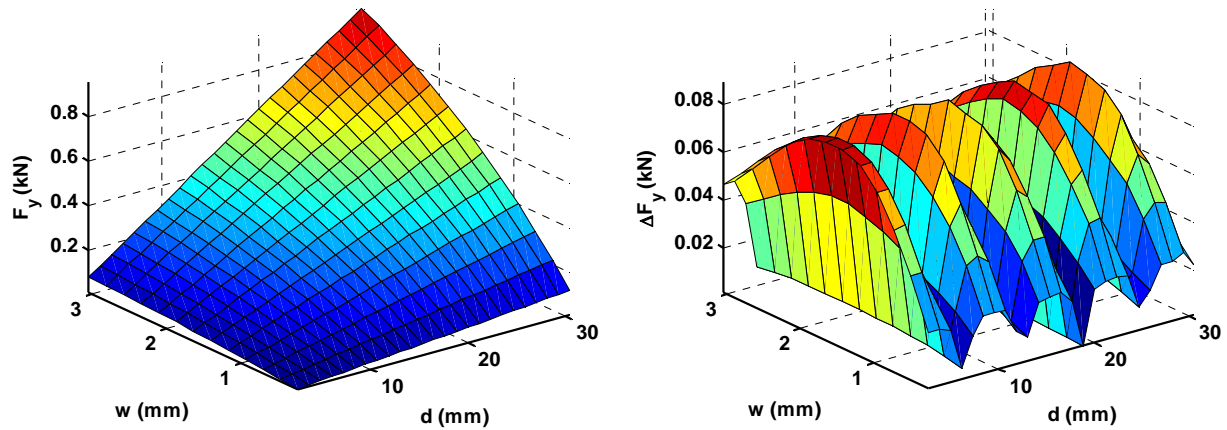

Figure 22: Maximum Absolute Value of *y* Force (left) and Peak–to–Peak *y* Force (right) as Functions of Width–of–Cut and Depth–of–Cut: N_s = 1750 rpm, N_f = 8, R_t = 9.525 mm, f_f = 0.051 mm/flute, and γ_r = 50°.

6. Process Planning

A process planning scheme for peripheral milling of thin titanium parts is given in this section. The material to remove has a cross section with a total depth–of–cut (d_t) and total width–of–cut (w_t). In this scheme the spindle speed, tool radius, and number of flutes is fixed. However, the scheme can be expanded to include these variables as well. The machining operation has a constraint on geometric tolerances (±0.127 mm) and a desired material removal rate of 273.1 mm³/hr. However, the geometric tolerance constraint will be considered by a maximum y force constraint which is given by

$$F_{max} = 2.78 \cdot 0.127 = 0.3531 \text{ kN} \qquad (27)$$

where 2.78 is the stiffness, in kN/mm, of the weakest point on the plate and 0.127 is the geometric tolerance, in mm. This constraint will be utilized in the process planning scheme.

6.1 Process Planning Scheme

A maximum helix angle (γ_{max}) and a minimum helix angle (γ_{min}) are selected. In this study $\gamma_{max} = 50°$ and $\gamma_{min} = 5°$. Since the number of tool passes must be an integer number, the process planning scheme will consider combinations of depths–of–cut and widths–of–cut that are, respectively, d_t, $d_t/2$, $d_t/3$, etc. and w_t, $w_t/2$, $w_t/3$, etc. For a depth–of–cut/width–of–cut combination the minimum helix angle is selected and a bisection routine is used to determine the maximum feed such that the maximum y force constraint is not violated. The function used in the bisection routine is $F_{max} - F_{y,max}$ where $F_{y,max}$ is the maximum y force determined by simulation. The bisection routine uses an initial low feed of 0 mm/flute since this will definitely cause the function to be positive and an initial high feed of 25.4 mm/flute since this will definitely cause the function to be negative. The algorithm converges when the following condition is realized

Approved for public release; distribution unlimited.

$$\left| \frac{F_{y,\max} - F_{\max}}{F_{\max}} \right| < 0.01 \qquad (28)$$

The lower feed is selected to ensure the maximum y force constraint is not violated. The helix angle is incremented by $\Delta\gamma_r$ and the bisection routine is again used to determine the maximum feed such that the maximum y force constraint is not violated. In this study, $\Delta\gamma_r = 3°$. This procedure is continued until the maximum helix angle is utilized. For the depth–of–cut/width–of–cut combination, the optimal helix angle is determined to be the helix angle where the feed is maximum, since this will maximize the material removal rate, which is given by

$$MRR = wfdN_f N_s \qquad (29)$$

The procedure is applied to every combination of depth–of–cut and width–of–cut. The solutions are then checked, via time domain simulations for stability. The solution with the maximum material removal rate that is stable is then selected. Note tool wear and surface finish constraints are not considered in this process planning scheme. These will be incorporated in future studies. Also, the time to prepare for subsequent tool passes is not considered in the material removal rate computation.

6.2 Process Planning Scheme Test Case

The process planning scheme is applied to a test case where $d_t = 30.48$ mm, $w_t = 3.048$ mm, $R_t = 9.525$ mm, and $N_s = 1750$ rpm. Up to three passes in both the depth and width directions are considered. The results are shown in Table 3. This example has discernable trends with respect to the optimal material removal rate, helix angle, and feed. First, optimal material removal rate decreases as the width–of–cut decreases, and is insensitive to the depth–of–cut. Second, the optimal helix angle increases as the depth–of–cut decreases, and is insensitive to the width–of–

cut. The optimal feed increases as the width–of–cut and depth–of–cut decrease. In all nine cases, chatter did not occur. The results indicate that, from the perspective of material removal rate, the total width–of–cut should be taken. However, other aspects, particularly tool wear rate and surface finish, will also need to be taken into account. In general, the lower the feed, the better the surface finish, which would indicate the total depth–of–cut should be taken. Also, since multiple tool passes are not necessary, the time between tool passes, which was not taken into account, would not be required.

Table 3: Process Planning Scheme Test Case Results.

Case	d (mm)	w (mm)	f_t (mm/flute)	γ_r (deg)	MRR (mm³/hr)	Stable
1	30.48	3.048	$1.859 \cdot 10^{-2}$	14	37.59	Yes
2	15.24	3.048	$3.708 \cdot 10^{-2}$	26	37.59	Yes
3	10.16	3.048	$5.518 \cdot 10^{-2}$	38	37.34	Yes
4	30.48	1.524	$2.946 \cdot 10^{-2}$	14	29.72	Yes
5	15.24	1.524	$5.969 \cdot 10^{-2}$	26	29.97	Yes
6	10.16	1.524	$8.534 \cdot 10^{-2}$	38	28.70	Yes
7	30.48	1.016	$4.115 \cdot 10^{-2}$	26	27.69	Yes
8	15.24	1.016	$8.052 \cdot 10^{-2}$	26	27.18	Yes
9	10.16	1.016	0.1179	35	26.42	Yes

Time domain simulations conducted for Cases 1, 3, 4, and 7, and the *y* force, part displacement, and PSDs for these two signals are shown for these cases, respectively, in Figures 23, 24, 25, and 26. The power spectral densities of the *y* force and part deflection signals were computed for the last half of the data sets, which is during the steady state. The power spectral densities of the *y* force signals contain significant energy at 233 Hz, which is the flute passing frequency, and its first and second multiples. This is also true of the power spectral densities of the part deflection signals; however, there is also significant energy at four multiples of the flute

passing frequency. Since the power spectral densities only contained significant energy at the flute passing frequency and its multiples, chatter was not present during the operations. It can also be seen that the feed is adjusted such that the maximum absolute value of the y force during the steady state is approximately F_{max} and the part displacement is approximately 0.127 mm. When comparing the y forces in the simulations in this section to the y forces shown in Figures 14–18, it can be seen that the peak–to–peak variation in the y forces are smaller by an order of magnitude. Therefore, the process planning scheme naturally found the valleys in the peak–to–peak y forces discussed in the previous section.
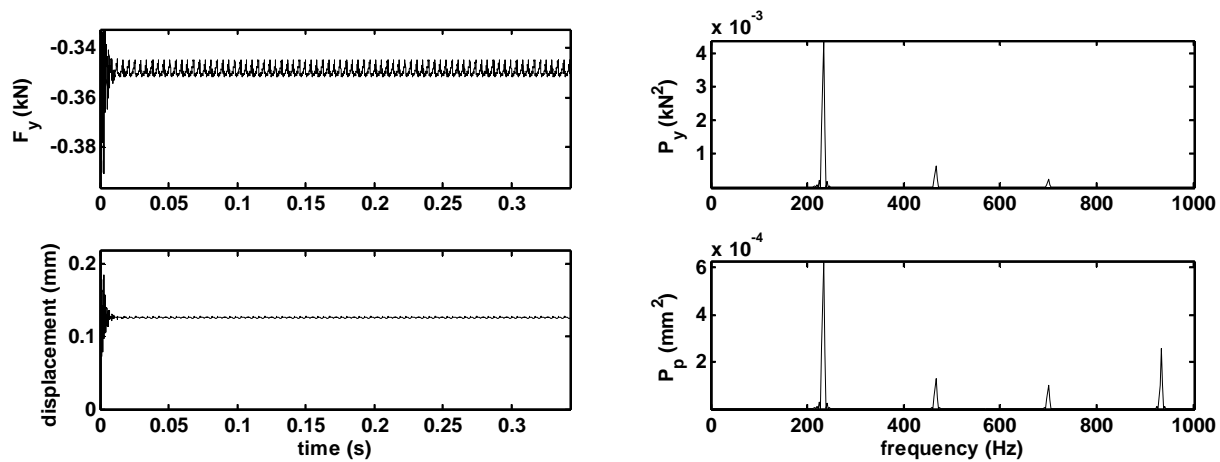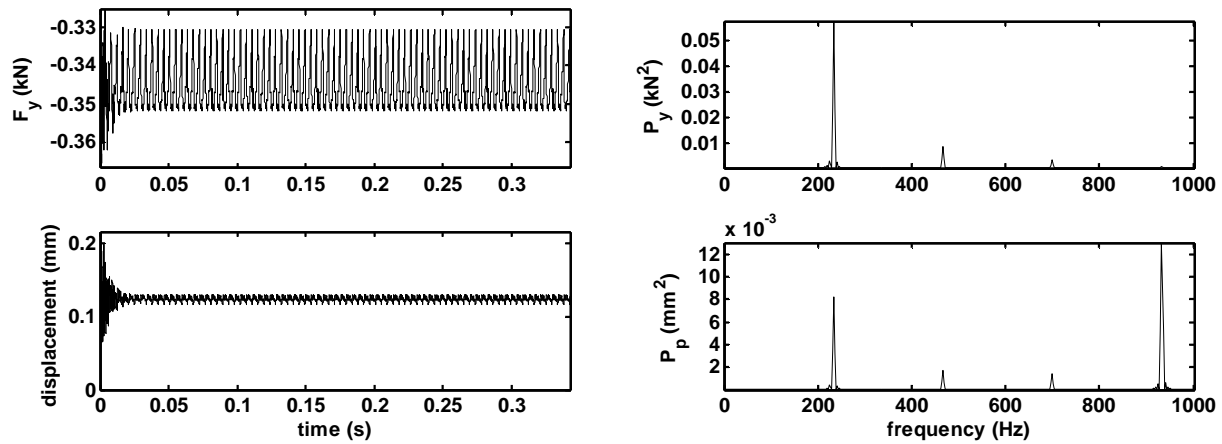

Figure 23: Time Domain Simulations (left) and Power Spectral Densities (right) of y Force and Part Displacement for Case 1 in Table 3: N_s = 1750 rpm, f_f = 1.859·10^{-2} mm/flute, w = 3.048 mm, d = 30.48 mm, γ_r = 14°, and MRR = 37.59 mm^3/hr.
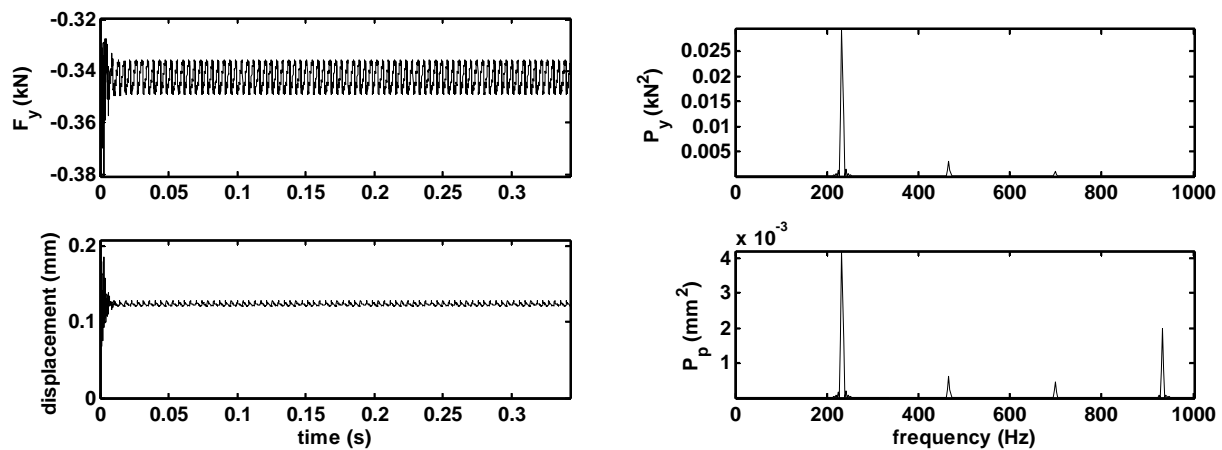
Figure 24: Time Domain Simulations (left) and Power Spectral Densities (right) of _y_ Force and Part Displacement for Case 3 in Table 3: N_s = 1750 rpm, f_f = 5.518·10^{-2} mm/flute, _w_ = 3.048 mm, _d_ = 10.16 mm, γ_r = 38°, and _MRR_ = 37.34 mm³/hr.

Figure 25: Time Domain Simulations (left) and Power Spectral Densities (right) of _y_ Force and Part Displacement for Case 4 in Table 3: N_s = 1750 rpm, f_f = 2.946·10^{-2} mm/flute, _w_ = 1.524 mm, _d_ = 30.48 mm, γ_r = 14°, and _MRR_ = 29.72 mm³/hr.
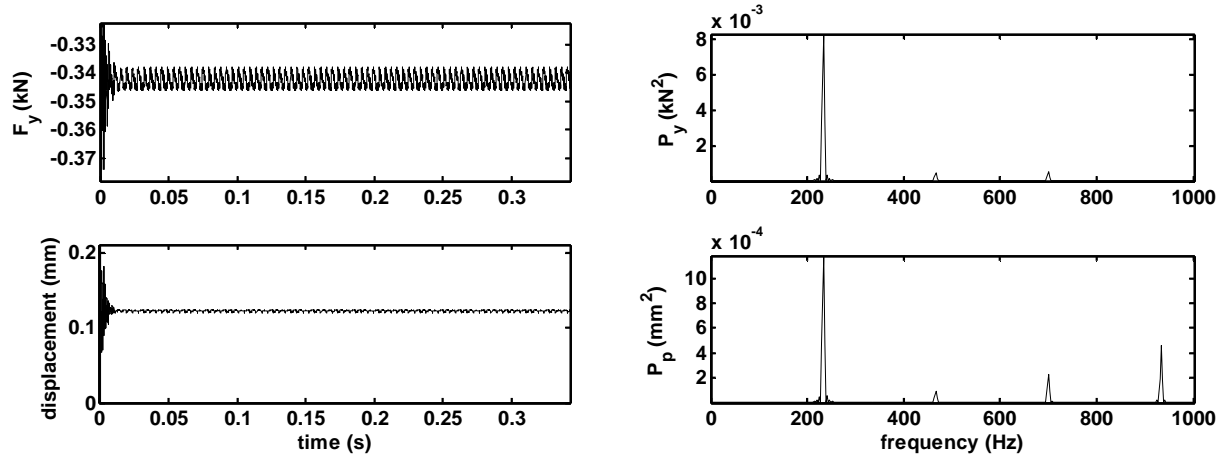
Figure 26: Time Domain Simulations (left) and Power Spectral Densities (right) of *y* Force and Part Displacement for Case 7 in Table 3: N_s = 1750 rpm, f_f = 4.115·10^{-2} mm/flute, *w* = 1.016 mm, *d* = 30.48 mm, γ_r = 26°, and *MRR* = 27.69 mm³/hr.

7. Summary and Conclusions

This paper described work that investigated the modeling and process planning of perferial milling operations for thin titanium parts. The equipment that was used in the experimental studies was described in detail. The Particle Swarm Optimization (PSO) method, which was used to model structural displacements and machining forces, was described and implemented. The structural models were compared to experimental data in the frequency and time domains. The machining force models were simulated and compared to experimental data generated by cutting a titanium block. The machining force models were combined with the structural models to simulate the machining of a thin titanium plate and simulation and experimental results were compared. A process planning scheme for the perferial milling of thin titanium parts was developed and a test case was conducted.

The PSO method was successful in creating machining force models and structural vibration models. The force models predicted the machining forces very well when machining thin plates. The structural models had some variation from the experimental results. This is believed to be due to the fact that the plate fixturing, which is slightly different each time a plate is put into the fixture, affects the structural models. The simulations showed that variations in the y force during a flute rotation were insensitive to width–of–cut, but are very sensitive to depth–of–cut and that for specific depths–of–cut the variation was virtually zero. The process planning test case revealed the optimal material removal rate decreases as the width–of–cut decreases, the optimal helix angle is independent of the width–of–cut, and the optimal feed increases as the width–of–cut decreases. The test case also revealed the optimal material removal rate is independent of depth–of–cut, the optimal helix angle increases as the depth–of–cut decreases, and the optimal feed increases depth–of–cut decreases.

Acknowledgement

References

Baeker, M., Roesler, J., and Siemers, C., 2000, "Chip Formation of Titanium Alloys at High Cutting Speeds," *Annals DAAAM*, Vol. 11, No. 21, pp. 15–16.

Barry, J., Byrne, G., and Lennon, D., 2001, "Observations on Chip Formation and Acoustic Emission in Machining Ti–6Al–4V Alloy," *International Journal of Machine Tools and Manufacture*, Vol. 41, No. 7, pp. 1055–1070.

Brinksmeier, E., Janssen, A.W.R., and Diersen, P., 1999, "Aspects of Cooling Lubrication Reduction in Machining Advanced Materials," *Proceedings of the Institution of Mechanical Engineers – Part B*, Vol. 213, No. B8, pp. 769–778.

Chen, M., Liu, G., Sun, F., Jian, X., and Yuan, R., 2002, "Investigation of Chip Formation Mechanism and Surface Integrity in High Speed Milling Titanium Alloy," *Key Engineering Materials*, Vol. 233–236, pp. 489–496.

Corduan, N., Himbert, T., Poulachon, G., Dessoly, M., Lambertin, M., Vigneau, J., and Payoux, B., 2003, "Wear Mechanisms of New Tool Materials for Ti–6Al–4V High Performance Machining," *Annals of the CIRP*, Vol. 52/1, pp. 73–76.

de Lacalle, L.N.L., Perez, J., Llorente, J.I., and Sanchez, J.A., 2000, "Advanced Cutting Conditions of the Milling of Aeronautical Alloys," *Journal of Materials Processing Technology*, Vol. 100, No. 1, pp. 1–11.

Hong, S.Y., Ding, Y., and Jeong, W–C., 2001a, "Friction and Cutting Forces in Cryogenic Machining of Titanium Ti–6Al–4V," *International Journal of Machine Tools and Manufacture*, Vol. 41, No. 15, pp. 2271–2285.

Hong, S.Y., Markus, I., and Jeong, W–C., 2001b, "New Cooling Approach and Tool Life Improvement in Cryogenic Machining of Titanium Alloy Ti–6Al–4V," *International Journal of Machine Tools and Manufacture*, Vol. 41, No. 15, pp. 2245–2260.

Kennedy, J. and Eberhart, R., 1995, "Particle Swarm Optimization," *IEEE International Conference on Neural Networks*, pp. 1942–1948.

Kuljanic, E., Fioretti, M., Beltrame, L., and Miani, F., 1998, "Milling Titanium Compressor Blades with PCD Cutter," *Annals of the CIRP*, Vol. 47/1, pp. 61–64.

Li, L., Chang, H., Wang, M., Zuo, D.W., and He, L., 2004, "Temperature Measurement in High Speed Milling Ti6Al4V," *Key Engineering Materials*, Vol. 258–259, pp. 804–484.

Li, R., Hegde, P., and Shih, A.J., 2007, "High–Throughput Drilling of Titanium Alloys," *International Journal of Machine Tools and Manufacture*, Vol. 47, No. 1, pp. 63–74.

Malone, T., 1997, "Tip on Tackling Tough Materials," *American Machinist*, Vol. 141, No. 11, pp. 56–62.

Shivpuri, R., Hua, J., Mittal, P., and Srivastava, A.K., 2002, "Microstructure–Mechanics Interaction in Modeling Chip Segmentation during Titanium Machining," *Annals of the CIRP*, Vol. 51/1, pp. 71–74.

Smith, S. and Tlusty, J., 1993, "Efficient Simulation Programs for Chatter in Milling," *Annals of the CIRP*, Vol. 42/1, pp. 463–466.

Tsai, M.D., Takata, S., Inui, M., Kimura, F., and Sata, T., 1990, "Prediction of Chatter Vibration by Means of a Model–Based Cutting Simulation System," *Annals of the CIRP*, Vol. 39/1, pp. 447–450.

Wang, Z.G., Wong, Y.S., and Rahman, M., 2005, "High Speed Milling of Titanium Alloys using Binderless CBN Tools," *International Journal of Machine Tools and Manufacture*, Vol. 45, No. 1, pp. 105–114.

Weck, M., Altintas, Y., and Beer, C., 1994, "CAD Assisted Chatter–Free NC Tool Path Generation in Milling," *International Journal of Machine Tools and Manufacture*, Vol. 34, No. 6, pp. 879–891.

Xu, J.H., Ren, K.Q., and Geng, G.S., 2004, "Cutting Forces in High–Speed Milling of a Close Alpha Titanium Alloy," *Key Engineering Materials*, Vol. 258–259, pp. 451–455.

Zoya, Z.A. and Krishnamurthy, R., 2000, "Performance of CBN Tools in the Machining of Titanium Alloys," *Journal of Materials Processing Technology*, Vol. 100, No. 1, pp. 80–86.